NURBS-Enhanced Finite Element Method (NEFEM)

Ruben Sevilla, Sonia Fernández-Méndez and Antonio Huerta*

Laboratori de Càlcul Numèric (LaCàN), Departament de Matemàtica Aplicada III,
E.T.S. de Ingenieros de Caminos, Canales y Puertos,
Universitat Politècnica de Catalunya,
Jordi Girona 1, E-08034 Barcelona, Spain
e-mail: {ruben.sevilla,sonia.fernandez,antonio.huerta}@upc.edu, web http://www-lacan.upc.edu

SUMMARY

An improvement of the classical finite element method is proposed. It is able to exactly represent the geometry by means of the usual CAD description of the boundary with Non-Uniform Rational B-Splines (NURBS). Here, the two-dimensional case is presented. For elements not intersecting the boundary, a standard finite element (FE) interpolation and numerical integration is used. But elements intersecting the NURBS boundary need a specifically designed piecewise polynomial interpolation and numerical integration. A priori error estimates are also presented. Finally, some examples demonstrate the applicability and benefits of the proposed methodology. NEFEM is at least one order of magnitude more precise than the corresponding isoparametric FE in every numerical example shown. This is the case for both continuous and discontinuous Galerkin formulations. Moreover, for a desired precision NEFEM is also more computational efficient, as shown in the numerical examples. The use of NEFEM is strongly recommended in the presence of curved boundaries and/or when the boundary of the domain has complex geometric details. The possibility of computing accurate solution with coarse meshes and high order interpolations, makes NEFEM a more efficient strategy than classical isoparametric FE. Copyright © 2000 John Wiley & Sons, Ltd.

KEY WORDS: NURBS; Finite Elements; CAD; Discontinuous Galerkin; exact geometry representation; high-order isoparametric finite elements; transient Maxwell equations

1. INTRODUCTION

The relevance of an accurate representation of the domain and its boundary has been pointed out by several authors, see [1, 2, 3, 4, 5, 6] among others. In some applications, such as compressible flow problems, if a Discontinuous Galerkin (DG) formulation is adopted, see [7], an important loss of accuracy is observed when a linear approximation of the boundary

---

*Correspondence to: Laboratori de Càlcul Numèric (LaCàN), E.T.S. Ingenieros de Caminos, Universitat Politècnica de Catalunya, Jordi Girona 1, E-08034 Barcelona, Spain.

is used, see [1, 2]. Bassi and Rebay [1] show that, in the presence of curved boundaries, a meaningful high-order accurate solution can only be obtained if the corresponding high-order approximation of the geometry is employed (i.e. isoparametric finite elements). In fact, it is necessary to take into account the boundary curvature effect in order to have a consistent boundary discretization, see [5]. In [6] the same problem is studied, and a new method is proposed for computing the flux across a curved face. Using a parametrization of the curved boundary the flux definition is modified but the resulting method is, unfortunately, non-conservative. The importance of the geometrical model in the numerical solution of compressible Euler equations is not exclusive of DG methods. In [2, 8] the problem is identified in the context of Finite Volume (FV) methods, and more recent advances in this area can be found in [9, 10].

An accurate representation of the geometry is not a prerogative of fluid mechanics. For instance, similar conclusions are derived in [3] for linear elasticity problems: sizable errors are present in the numerical solution when the order for the geometric approximation is lower than the order of functional interpolation, even for geometries as simple as a sphere. Isoparametric finite elements (FE) or superparametric FE are necessary in order to ensure an accurate enough representation of the geometry. The relevance of an accurate geometric model for some applications in solid mechanics is also illustrated in [11], where the use of B-Splines is proposed for the geometric representation of the interface in frictionless contact problems.

Obviously, Maxwell equations are also very sensitive to the quality of the boundary representation. Reference [4] studies the error induced by the approximation of curvilinear geometries with isoparametric elements. The 3D Maxwell equations are solved in a sphere with isoparametric FE and with an exact mapping of the geometry. The exact mapping provides more accurate results with errors differing by an order in magnitud. Thus, in some applications, an isoparametric representation of the geometry is far from providing an optimal numerical solution for a given FE discretization.

Recently, [12] proposes a new methodology: the *isogeometric analysis*. Its goal is to consider an exact representation of the geometry, with no dependency on the spatial discretization. In the *isogeometric analysis* the solution of the boundary value problem is also approximated with the same NURBS (*Non-Uniform Rational B-Splines*, [13]) basis used for the description of the geometry. This idea was first introduced in [14] in the context of thin shell analysis, but using *subdivision surfaces* instead of NURBS.

The methodology proposed in this paper has a similar goal: an exact representation of the geometry, but it is simpler because NURBS are restricted to the boundary of the computational domain. Only the boundary of the computational domain is directly related to a CAD. Thus, *NURBS-Enhanced Finite Element Method* (NEFEM) considers the exact NURBS description for the boundary of the computational domain while the solution is approximated with a standard piecewise polynomial interpolation. Moreover, in the large majority of the domain (namely in the interior, that is for elements not intersecting the boundary) a standard FE interpolation and numerical integration is used, preserving the computational efficiency of classical FE techniques.

The use of a piecewise polynomial approximation represents an important advantage in front of the NURBS functional approximation used in the *isogeometric analysis*. NEFEM ensures local reproducibility of polynomials and, therefore, it preserves the classical FE convergence properties and allows a seamless coupling with the standard FE of the domain interior.

Section 2 introduces the basic concepts on NURBS. In section 3 the fundamentals of NEFEM

are presented. Special attention is paid to the interpolation and numerical integration in those elements affected by the NURBS description of the boundary. To simplify the presentation and show its capabilities NEFEM is presented for 2D domains. The generalization to 3D domains is conceptually easy but requires some extra attention to geometrical aspects and it will be the scope of a forthcoming publication. Some comments on the implementation of NEFEM are given and a priori error estimates are also presented in section 3. Numerical examples are discussed in section 4. NEFEM can be implemented with a standard piecewise continuous (standard FE) or discontinuous (DG) formulation. Thus, a Poisson problem is solved first in a continuous framework and several electromagnetic scattering problems are solved using DG. Application to fluid mechanics can be found in [15], where the advantages of NEFEM for the simulation of compressible flow problems are shown for both linear and high-order approximations.

2. BASIC CONCEPTS ON NURBS

A qth-degree NURBS curve [13] is a piecewise rational function defined in parametric form as

$$\boldsymbol{C}(\lambda) = \left(\sum_{i=0}^{n_{cp}} \nu_i \, \boldsymbol{B}_i \, C_{i,q}(\lambda) \right) \Bigg/ \left(\sum_{i=0}^{n_{cp}} \nu_i \, C_{i,q}(\lambda) \right) \qquad 0 \leq \lambda \leq 1, \tag{1}$$

where $\{\boldsymbol{B}_i\}$ are the coordinates of the $n_{cp} + 1$ *control points* (forming the *control polygon*), $\{\nu_i\}$ are the control weights, and the $\{C_{i,q}(\lambda)\}$ are the normalized B-spline basis functions of degree q, which are defined recursively as

$$C_{i,0}(\lambda) = \begin{cases} 1 & \text{if } \lambda \in [\lambda_i, \lambda_{i+1}[, \\ 0 & \text{elsewhere}, \end{cases}$$

$$C_{i,k}(\lambda) = \frac{\lambda - \lambda_i}{\lambda_{i+k} - \lambda_i} C_{i,k-1}(\lambda) + \frac{\lambda_{i+k+1} - \lambda}{\lambda_{i+k+1} - \lambda_{i+1}} C_{i+1,k-1}(\lambda),$$

for $k = 1 \ldots q$, where λ_i, for $i = 0, \ldots, n_k$, are the *knots* or *breakpoints*, which are assumed ordered $0 \leq \lambda_i \leq \lambda_{i+1} \leq 1$. They form the so-called *knot vector*

$$\Lambda = \{\underbrace{0, \ldots, 0}_{q+1}, \lambda_{q+1}, \ldots, \lambda_{n_k - q - 1}, \underbrace{1, \ldots, 1}_{q+1}\},$$

which uniquely describes the B-spline basis functions. The multiplicity of a knot, when it is larger than one, determines the decrease in the number of continuous derivatives. Control points, $n_{cp}+1$, and knots, n_k+1, are related to the degree of the parametrization, q, by the relation $n_k = n_{cp} + q + 1$, see [13] for more details. Figure 1 shows the B-spline basis functions for the knot vector

$$\Lambda = \{0, 0, 0, 0.2, 0.4, 0.6, 0.8, 0.8, 1, 1, 1\}. \tag{2}$$

Note that NURBS are piecewise (rational) functions and their definition changes at knots.

An example of a NURBS curve is represented in Figure 2 with the corresponding control polygon. The image of the breakpoints or knots by the NURBS are depicted in order to stress the discontinuous definition of the parametrization. In practice CAD manipulators work with *trimmed* NURBS, which are defined as the initial parametrization restricted to a subspace of the parametric space. Figure 3 shows the NURBS curve of Figure 2 trimmed to the subinterval $[0.05, 0.75]$.
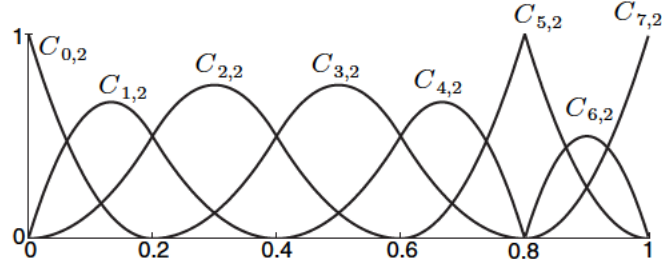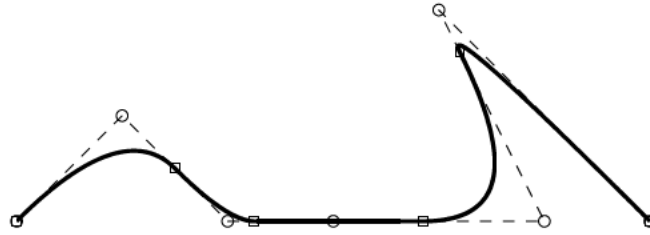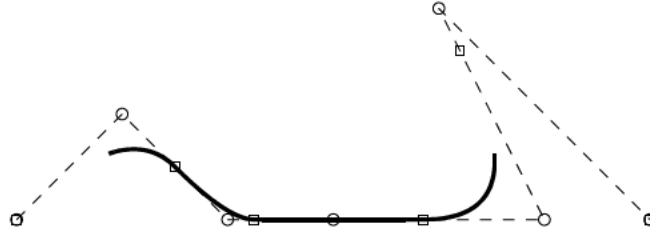
Figure 1. B-spline basis functions for the knot vector (2)

Figure 2. NURBS curve (solid line), control points (denoted by ∘), control polygon (dashed line) and breakpoints (denoted by □)

Figure 3. Trimmed NURBS curve with $\lambda \in [0.05, 0.75]$ (solid line), control points (denoted by ∘), control polygon (dashed line) and breakpoints (denoted by □)

3. NURBS-ENHANCED FINITE ELEMENT METHOD (NEFEM)

Consider a physical domain $\Omega \subset \mathbb{R}^2$ whose boundary $\partial\Omega$, or a portion of it, is defined by NURBS curves. Every NURBS is assumed to be parametrized by

$$C : [0, 1] \longrightarrow C([0, 1]) \subseteq \partial\Omega \subset \mathbb{R}^2.$$

A regular partition of the domain $\overline{\Omega} = \bigcup_e \overline{\Omega}_e$ in triangles is assumed such that every element Ω_e has at most one side, Γ_e, on the NURBS boundary. Figure 4 shows a domain with part of the boundary described by a NURBS curve corresponding to the NACA 0012 airfoil, and a valid triangulation for NEFEM.

As usual in FE mesh generation codes, it is assumed that every curved boundary side belongs to a unique NURBS, $\Gamma_e \subseteq C([0, 1])$. That is, one element edge can not be defined by portions
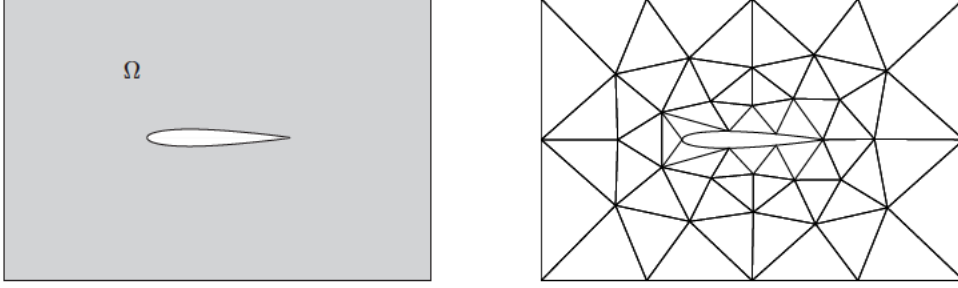
Figure 4. Physical domain with part of the boundary defined by a NURBS curve (left) and a valid triangulation for the NEFEM (right)

of two (or more) different NURBS curves. But on the contrary, it is important to note that breakpoints, which characterize the piecewise nature of NURBS, are independent of the mesh discretization. Thus, the NURBS parametrization can change its definition inside one side, that is breakpoints may belong to element sides and do not need to coincide with FE nodes. This is another major advantage with respect to the isogeometric analysis [12].

Every *interior* element (i.e. elements not having an edge that coincides with the NURBS boundary) can be defined and treated as standard FE or DG elements. Therefore, in the vast majority of the domain, interpolation and numerical integration are standard. This section is devoted to the definition of the interpolation and the numerical integration at an element with one side, Γ_e, along the NURBS boundary. Say Ω_e is an element with two straight interior edges and one side defined by a trimmed NURBS,

$$\Gamma_e = C([\lambda_1^e, \lambda_2^e]),$$

where λ_1^e and λ_2^e are the parametric coordinates (in the parametric space of the NURBS) of the end points of Γ_e; obviously they must verify $0 \leq \lambda_1^e < \lambda_2^e \leq 1$.

For each element Ω_e, a straight-sided triangle T_e is defined using its vertices, see Figure 5. A linear mapping $\boldsymbol{\Psi} : I \longrightarrow T_e$ is used, which goes from the reference triangle I to the triangle T_e, see Figure 6. The inverse of this linear transformation maps the triangle T_e into the reference triangle I and, more important, also maps the actual element Ω_e, which is in the physical domain, into a curved element in local coordinates with two straight sides, namely

$$I_e := \boldsymbol{\Psi}^{-1}(\Omega_e),$$

see Figure 7. I_e is called the *local curved element* for the actual element Ω_e.

Note that the reference triangle I is the same for all elements Ω_e. However, the local curved element I_e depends on the trimmed NURBS defining the curved side Γ_e of Ω_e, and therefore it is different for every element Ω_e intersecting the NURBS boundary.

Remark 1. *In order to simplify the presentation, it is assumed that the interior vertex of T_e is mapped to the vertex $(-1, 1)$ in I. The implementation of this condition only requires a proper local numbering of the vertices of the element.*

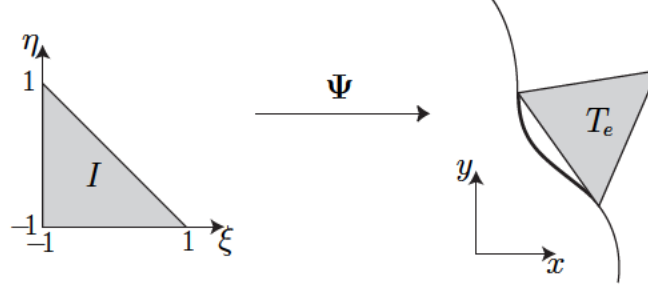Figure 5. Actual element Ω_e (left) and triangle T_e defined using its vertices (right) in the physical domain

Figure 6. Mapping Ψ defined as a linear transformation from the reference triangle I to the straight-sided triangle T_e in the physical domain
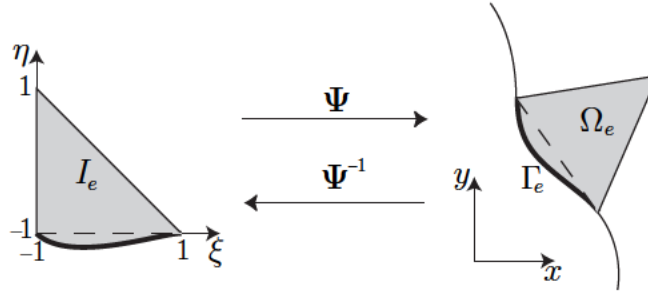

Figure 7. The linear transformation also maps the local curved element I_e to the actual element Ω_e in the physical domain

3.1. FE polynomial basis

In order to work with standard FE polynomial approximations, Lagrange polynomials (that is, standard nodal interpolation) can be considered. In fact, they can be defined on the curved triangle, I_e, in the reference domain or equivalently, in the actual element in the physical domain, Ω_e. The use of a linear transformation from local (reference) coordinates $\boldsymbol{\xi} = (\xi, \eta)^T$ in I_e to cartesian coordinates $\boldsymbol{x} = (x, y)^T$ in Ω_e, ensures that a complete polynomial interpolation of degree m in $\boldsymbol{\xi}$ leads to a polynomial interpolation with the same degree in $\boldsymbol{x}$. Thus, consistency and accuracy of the approximation is ensured even for elements Ω_e far from being a straight-sided element.

To make the computation of Lagrange polynomials more systematic, for any degree and for any distribution of nodes, the implementation proposed in [16] is adopted. A polynomial basis $\{P_i(\boldsymbol{\xi})\}$, with the required degree and whose definition is independent of the nodal coordinates,
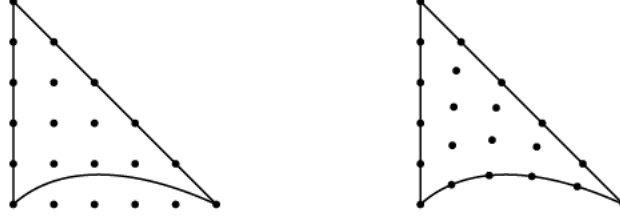
Figure 8. 5th-order nodal distributions in I_e: for equally-spaced nodes in the straight-side triangle (left) and adapted to the NURBS side (right)
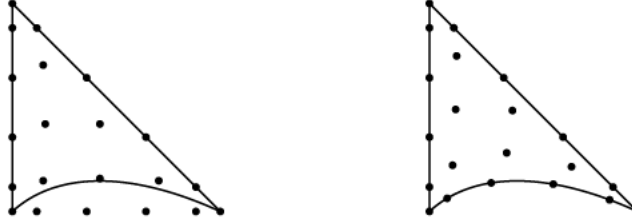

Figure 9. 5th-order nodal distributions in I_e: Fekete nodes in the straight-side triangle (left) and adapted to the NURBS side (right)

is considered. Then, given a nodal distribution in I_e, with coordinates $\{\boldsymbol{\xi}_i\}_{i=1}^{\mathbf{n_{en}}}$, the Lagrange polynomial basis $\{L_i(\boldsymbol{\xi})\}_{i=1}^{\mathbf{n_{en}}}$ can be expressed in terms of the polynomial basis $\{P_i(\boldsymbol{\xi})\}_{i=1}^{\mathbf{n_{en}}}$ as

$$L_i(\boldsymbol{\xi}) = \sum_{j=1}^{\mathbf{n_{en}}} \left[V^{-1}\right]_{ji} P_j(\boldsymbol{\xi}), \tag{3}$$

where $\mathbf{n_{en}}$ is the number of element nodes and the multidimensional Vandermonde matrix is defined as $V_{ij} := P_j(\boldsymbol{\xi}_i)$, for $i, j = 1, \ldots, \mathbf{n_{en}}$.

Remark 2. *Note that equation (3) holds for any polynomial basis $\{P_i(\boldsymbol{\xi})\}_{i=1}^{\mathbf{n_{en}}}$. Here an orthogonal polynomial basis $\{P_i(\boldsymbol{\xi})\}_{i=1}^{\mathbf{n_{en}}}$ derived from the Jacobi polynomials is considered, to ensure moderate condition number for the Vandermonde matrix V, see [16] and references therein. Moreover, orthogonal polynomial basis allows analytical evaluation of some inner products in straight-sided elements [17].*

From an implementation point of view, it is worth noting that all element matrices can be first computed for any polynomial basis, and then transformed with the Vandermonde matrix. That is, let M_e^p be an element matrix computed in terms of the polynomial basis $\{P_i(\boldsymbol{\xi})\}_{i=1}^{\mathbf{n_{en}}}$, then $M_e = V^{-T} M_e^p V^{-1}$ is the corresponding element matrix for the Lagrange nodal basis $\{L_i(\boldsymbol{\xi})\}_{i=1}^{\mathbf{n_{en}}}$.

Different options can be considered for the definition of a nodal distribution in I_e. If low-order elements are used, which is the standard approach in FE, equally-spaced nodal distributions on the straight-side triangle can be implemented directly, see Figure 8. When high-order elements are used for high-fidelity computations, as it is standard in DG methods, it is more convenient to use special distributions of nodes in order to reduce the condition number of the
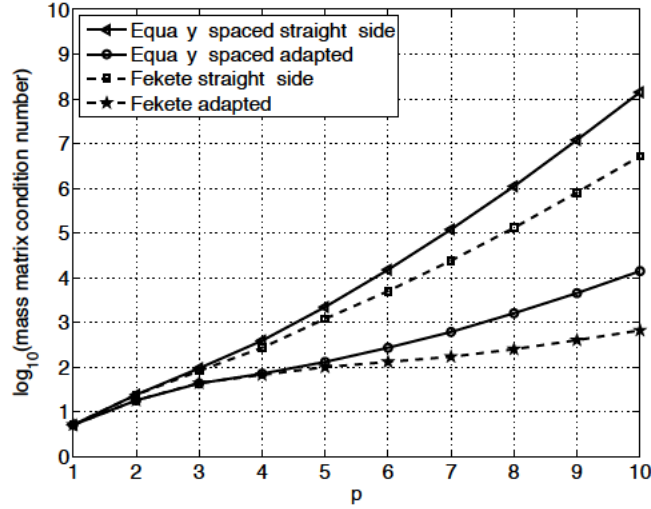
Figure 10. Condition number of the mass matrix as a function of the interpolation degree (p), using equally-spaced nodal distributions and Fekete points

resulting element matrices, see [18, 19] for details. Fekete points [20] are a good example of such distributions, see Figure 9.

The definition of a nodal distribution on the straight-side triangle, see left distributions in Figures 8 and 9, induces a marginal extra efficiency, because there is both a unique definition of nodal coordinates and only one computation of the Vandermonde matrix (independently of the curved element). Another alternative is to adapt the nodal distribution to the exact geometry, see right distributions in Figures 8 and 9. This option is more reasonable when nodal values are prescribed along the boundary. On the other hand, nodal distributions adapted to the boundary do not represent any relevant advantage if boundary conditions are imposed in weak form, as usual in DG formulations. Note however, the evolution of the condition number shown in Figure 10 for the element mass matrix as a function of the interpolation degree. As expected, Fekete points clearly decrease the condition number but adapted distributions of nodes also have a major influence on the condition number.

3.2. Numerical integration

The weak form that must be solved requires both integrations along element edges and in the elements interiors. All integrals in elements not having an edge along the NURBS boundary are computed using standard procedures. The elements Ω_e with one side, Γ_e, on the NURBS boundary require special attention. Two cases must be considered: line integrals (usually related to the implementation of natural boundary conditions or to flux evaluation along Γ_e in a DG context) or surface integrals (standard integrals in the element Ω_e). As discussed in the previous section, since NEFEM uses polynomials to approximate the solution, the difficulties in numerical integration are only restricted to the definition of a proper numerical quadrature in the curved element $I_e = \Psi^{-1}(\Omega_e)$ or its corresponding curved face. This, as will be observed below, reduces the complexity in the accurate evaluation of integrals, which are not as costly
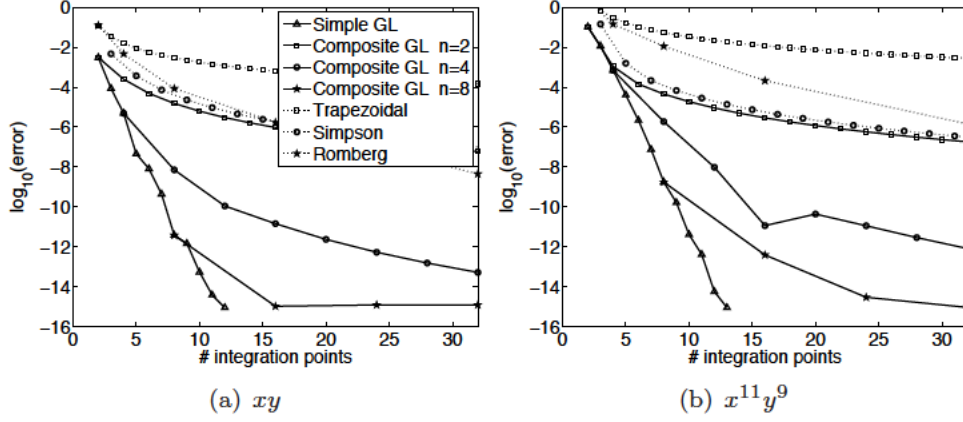
(a) xy (b) $x^{11}y^9$

Figure 11. Relative error for the integration of polynomials xy and $x^{11}y^9$ along the front part of the NACA 0012 airfoil.

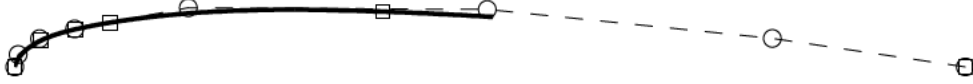Figure 12. Trimmed NURBS curve describing the front part of the NACA 0012 airfoil (solid line), control points (○), control polygon (dashed line) and image of the breakpoints (□)

as in standard mesh-free methods [21], or in isogeometric analysis [12].

3.2.1. Line integrals A line integral to be computed along a curved boundary side given by a trimmed NURBS, $\Gamma_e = C([\lambda_1^e, \lambda_2^e])$, can be written as

$$\int_{\Gamma_e} f \, d\ell = \int_{\lambda_1^e}^{\lambda_2^e} f\big(C(\lambda)\big) \, \|J_C(\lambda)\| \, d\lambda,$$

where f is a generic function (usually polynomial), and $\|J_C\|$ denotes the norm of the differential of the NURBS parametrization C (which, in general, is not a polynomial). As usual, a 1D numerical quadrature is used for the numerical computation of the integral, namely

$$\int_{\Gamma_e} f \, d\ell \approx \sum_{i=1}^{n_{ip}} f\big(C(\lambda_i)\big) \, \|J_C(\lambda_i)\| \, \omega_i, \tag{4}$$

where λ_i and ω_i are the coordinates and weights of the n_{ip} integration points in $[\lambda_1^e, \lambda_2^e]$.

Recall that the parametrization of a trimmed NURBS, C, is a piecewise rational function whose definition changes at breakpoints. Thus, an independent numerical quadrature must be considered at every interval between breakpoints (patch) to account for the discontinuous nature of the parametrization. In [22] a detailed comparison and discussion on different alternatives to evaluate (4) is presented. Numerical experiments reveal that Gauss-Legendre quadratures are a competitive choice in front of other quadrature rules such as trapezoidal and Simpson composite rules or Romberg's integration. For instance, Figure 11 shows the evolution of the relative error for the integration of polynomials xy and $x^{11}y^9$ along the trimmed NURBS

corresponding to the front part of the NACA 0012 airfoil, see Figure 12. For Gauss-Legendre composite rules, $\mathtt{n}$ denotes the number of integration points in every subinterval. Note that a composite quadrature with two intervals and $\mathtt{n} = 8$ Gauss-Legendre integration points in each interval achieves almost machine precision. Thus, although the faster convergence is obviously obtained for high-order simple quadratures (in each patch), the use of composite rules is very attractive, because it allows the definition of adaptive quadratures to control the integration error and ensure reliable computations for any NURBS and any order of polynomial interpolation.

Remark 3. *It is worth noting that in practical applications it is not necessary to compute numerical integrals with machine precision. Numerical experiments simulating the scattering of a planar electromagnetic wave [22] reveal that, in practice, if the NURBS is parametrized such that velocity has smooth variations, only one extra integration point, compared to standard isoparametric FE, is required. That is, for a given discretization with polynomials of order p, a numerical quadrature with p + 2 Gauss-Legendre integration points in each patch provides the maximum accuracy.*

3.2.2. Element integrals   NEFEM also requires to compute integrals in an element Ω_e with one side Γ_e on the NURBS boundary, see Figure 7. That is,

$$\int_{\Omega_e} f \, dx \, dy = |J_{\boldsymbol{\Psi}}| \int_{I_e} f \, d\xi \, d\eta \tag{5}$$

where $|J_{\boldsymbol{\Psi}}|$ is the determinant of the Jacobian of the linear transformation $\boldsymbol{\Psi}$. Thus, a numerical quadrature for every local curved element I_e is needed. In [22] different alternatives are presented and discussed. The best alternative, see Figure 13, is to define a transformation from the rectangle $[\lambda_1^e, \lambda_2^e] \times [0, 1]$ to the curved element I_e, namely,

$$\begin{aligned}
\boldsymbol{\varphi} : [\lambda_1^e, \lambda_2^e] \times [0, 1] &\longrightarrow I_e \\
(\lambda, \zeta) &\longmapsto \begin{Bmatrix} \varphi_1 \\ \varphi_2 \end{Bmatrix} := \begin{Bmatrix} \phi_1(\lambda)(1 - \zeta) - \zeta \\ \phi_2(\lambda)(1 - \zeta) + \zeta \end{Bmatrix}
\end{aligned} \tag{6}$$

where $\boldsymbol{\phi} = (\phi_1, \phi_2)^T := \boldsymbol{\Psi}^{-1} \circ \boldsymbol{C}$ is the parametrization of the trimmed NURBS corresponding to the curved side in I_e. Note that this transformation requires that nodes are numbered following the non restrictive assumption presented in Remark 1. Note also, that such a parametrization is linear in ζ and, as discussed in Remark 4, this implies important practical advantages. Thus, using the transformations shown in Figure 13, integral (5) is computed as

$$\int_{\Omega_e} f \, dx \, dy = |J_{\boldsymbol{\Psi}}| \int_{I_e} f \, d\xi \, d\eta \simeq |J_{\boldsymbol{\Psi}}| \sum_{i=1}^{\mathtt{n_{ip}}} \sum_{j=1}^{\mathtt{m_{ip}}} f(\boldsymbol{\xi}_{ij}) |J_{\boldsymbol{\varphi}}(\lambda_i, \zeta_j)| \, \omega_i \varpi_j \tag{7}$$

where $\mathtt{n_{ip}}$ and $\mathtt{m_{ip}}$ are the number of integration points in λ and ζ directions, respectively, $\boldsymbol{\xi}_{ij} := \boldsymbol{\varphi}(\lambda_i, \zeta_j)$, $\{\lambda_i, \omega_i\}$ and $\{\zeta_j, \varpi_j\}$ are the 1D quadrature points and weights for $[\lambda_1^e, \lambda_2^e]$ and $[0, 1]$ respectively, and $|J_{\boldsymbol{\varphi}}|$ is the determinant of the Jacobian of the transformation $\boldsymbol{\varphi}$. Note that to integrate a polynomial f of degree k in Ω_e, given the transformations shown in Figure 13, the (non polynomial) function

$$\widetilde{f}(\lambda, \zeta) = f\big(\boldsymbol{\varphi}(\lambda, \zeta)\big) |J_{\boldsymbol{\varphi}}(\lambda, \zeta)|. \tag{8}$$
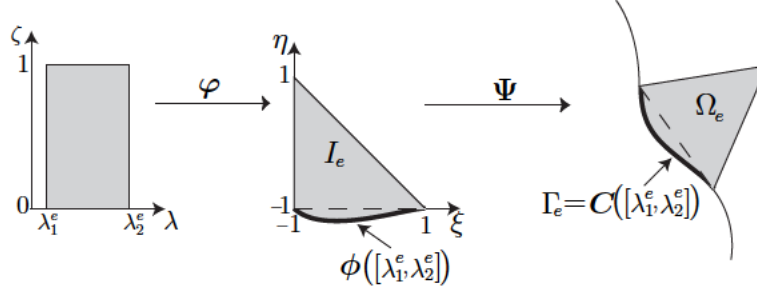
Figure 13. Transformation from $[\lambda_1^e, \lambda_2^e] \times [0, 1]$ to I_e and Ω_e

must be integrated in $[\lambda_1^e, \lambda_2^e] \times [0, 1]$. Recall that φ, see (6), is linear in ζ and, therefore, $f(\varphi(\lambda, \zeta))$ is a polynomial of degree k in ζ. Moreover, $|J_\varphi(\lambda, \zeta)|$ is linear in ζ. Thus, $\widetilde{f}(\lambda, \zeta)$ is a polynomial of degree $k+1$ in ζ and consequently a Gauss-Legendre quadrature of order k (or $k+1$ for even k) is optimal for the 1D quadrature along ζ.

Remark 4. *When the transformation from the rectangle φ is considered, the integrals involved in the elemental matrices, for a NEFEM solution with interpolation of degree p, can be exactly computed for one of the parameters, ζ, using a Gauss-Legendre quadrature with $p+1$ integration points. The other dimension, λ, can be integrated using the same quadrature considered in section 3.2.1 for line integrals over NURBS.*

Note that the rational definition of application φ is only due to the rational definition of the boundary. Thus, in the particular case of a geometry given by a q-th degree B-spline, i.e. a piecewise polynomial parametrization, the elemental matrices can be exactly computed with Gauss-Legendre quadratures with $p+1$ integration points for the ζ parameter, and $q(p+1)$ integration points for the NURBS parameter λ. For instance, the NACA 0012 geometry is usually described by a B-Spline of degree $q = 3$, and therefore element integrals can be exactly computed with Gauss-Legendre quadratures with $p+1$ and $3(p+1)$ integration points in each direction.

Remark 5. *When the parametrization of the NURBS is smooth (i.e. for small variations of the so-called velocity of the parametrization), $p+1$ integration points (in each patch) for parameter λ are only required to achieve maximum accuracy in the quantity of interest. Thus, for NEFEM edges not including breakpoints, the number of integration points is the same as for standard isoparametric FE. This is illustrated in the numerical experiments simulating the scattering of a planar electromagnetic wave in [22] and the examples in section 4.1.*

Another obvious option instead of using φ to transform a rectangle into I_e, is to define another transformation from I to a curved triangle I_e and then use quadratures specifically designed for triangles. This is also discussed in [22]. For standard FE these triangle quadratures require less integration points than other quadrature rules to achieve the same accuracy, but this is not the case here. The use of a transformation depending on the NURBS parametrization (from I to a curved triangle) leads to expensive triangle quadratures. The integration strategy proposed in this section is much more competitive due to the good behavior of parameter ζ commented in Remark 4.
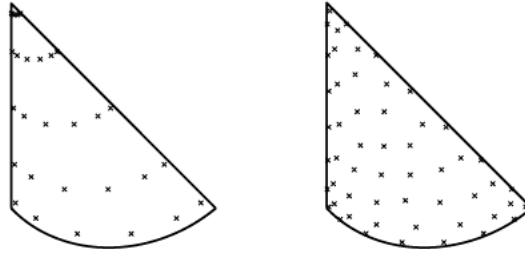
Figure 14. Two numerical quadratures in a curved element for the same accuracy

The efficiency of the proposed quadrature is illustrated in Figure 14. It shows the integration points required to integrate x over a curved triangle with an error of 0.5%, using the transformation from a rectangle proposed in this section (with 30 integration points) and a symmetric triangle quadrature [23] adapted to the curved element (with 54 integration points), see [22] for details.

3.3. Some comments on the implementation of the NEFEM

The enhancement of a standard FE code with the NEFEM methodology requires little effort. Note that the main difference of a NEFEM code with a standard FE code is at the level of the computation of elemental matrices and vectors for curved elements and edges. In fact, fortunately, the usual routines for the computation of elemental matrices and vectors for straight-sided elements can be directly used, without any modification, just using a modified definition of the reference element. That is, the integration points and the shape functions evaluated at these points, which are usually an input of these routines, have to be particularized for every local curved element I_e or side Γ_e. Thus, most of the routines usual in a standard FE code (routines for assembly, computation of elemental matrices and vectors, etc) can be directly used.

In fact, the most crucial point in the implementation may be the inclusion of the NURBS boundary information. The information for the evaluation of all NURBS describing the boundary has to be stored. Moreover, for every curved side $\Gamma_e = \mathbf{C}([\lambda_1^e, \lambda_2^e])$ the information of the corresponding trimmed NURBS is also necessary, that is, the extremes of the interval λ_1^e and λ_2^e and a pointer to the information of the NURBS $\mathbf{C}$. Nowadays this is not an information usually provided by standard mesh generators but, it is worth noting that routines for the evaluation of NURBS can be easily obtained or implemented [13].

On the other hand, in the context of DG formulations, NEFEM is a natural option for the implementation of high-order approximations in domains with curved boundaries. In DG codes it is usual to store only the vertices of a triangle mesh, and their connectivities, usually obtained with a linear triangle mesh generator. For high-order computations with straight-sided elements, if needed, all nodal coordinates are determined from the vertices coordinates. Under these circumstances NEFEM allows a straightforward implementation of curved boundaries, with no need of a high-order mesh generator, because the nodal coordinates at elements with one side on the NURBS boundary can be easily determined from the vertices of the triangles and the NURBS information.

3.4. A priori error estimates

Since NEFEM considers the usual FE polynomial interpolation, see section 3.1, a priori error estimates are exactly the same as those for standard FE. For instance, the result for the solution of second order elliptic problems is recalled in the following theorem.

Theorem 1. *Let $\mathcal{T}_h$ a non-degenerate triangulation (i.e. there is a positive constant β such that $\varrho_e/h_e \geq \beta$, for all $\Omega_e \in \mathcal{T}_h$, where h_e and ϱ_e are the diameters of Ω_e and of the circle inscribed in Ω_e, respectively). Assuming that all boundary conditions along curved boundaries are imposed in weak form, the following a priori estimate holds*

$$\|u - u_h\|_{\mathcal{L}^2(\Omega)} \leq K h^{p+1} |u|_{\mathcal{H}^{p+1}(\Omega)}, \tag{9}$$

where $u \in \mathcal{H}^{p+1}(\Omega)$ and u_h are the exact and the NEFEM solution respectively, K is a constant, h is the mesh size, and p is the polynomial degree of interpolation.

Moreover, for p-refinement convergence the following estimate also holds,

$$\|u - u_h\|_{E(\Omega)} \leq C \exp(-kN^r), \tag{10}$$

where $\|\cdot\|_{E(\Omega)}$ is the energy norm, C and k are positive constants, N is the number of degrees of freedom, and $r \gtrsim 1/2$ for 2D problems.

The same arguments used in the proof of standard FE error estimates are valid for the proof of Theorem 1. In fact, the derivation of a priori error estimates for NEFEM is identical to FE a priori estimates in polygonal domains, which can be found in [24, 25, 26] for h-refinement and in [27] for p-refinement.

It is worth noting that contrary to NEFEM, the proof of a priori error estimates for isoparametric FE in the presence of curved boundaries requires special attention. First, the use of isoparametric FE induces geometric errors because the computational domain is, in fact, a piecewise polynomial approximation of the physical geometry. Thus, to obtain optimal a priori error estimates, the maximum distance between the computational and the exact boundary should be bounded by γh^p, where γ is a constant, h is the mesh size and p is the polynomial degree. Moreover, bounds of the jacobian of the isoparametric transformation and its first p derivatives are also necessary, see [28]. Thus, an isoparametric curved element must verify two contradictory requirements. On one hand, the computational polynomial boundary has to be close enough to the curved boundary. And on the other hand, the discrepancy between the curved element and the straight element given by its vertices must vanish fast enough, see [29]. In practice, this requirements imply that specific nodal distributions on curved elements are mandatory in order to obtain the optimal rate of convergence. For instance, with cubic elements, small variations of the interior node cause suboptimal convergence.

With NEFEM (as well as for FE in a domain with polygonal boundary) the spatial discretization does not introduce geometric errors. Moreover, NEFEM uses a linear mapping to relate local and cartesian coordinates, see section 3. In fact, the linear transformation used by NEFEM is exactly the same mapping used by standard FE on a domain with polygonal boundaries. Consequently, all a priori error estimates demonstrated in FE for domains with polygonal boundaries can be reproduced exactly for NEFEM, even in the presence of elements far from having straight edges.

Theorem 1 assumes that essential boundary conditions are imposed in weak form, for instance with numerical fluxes in a DG context, or with Nitsche's method [30, 31] in a
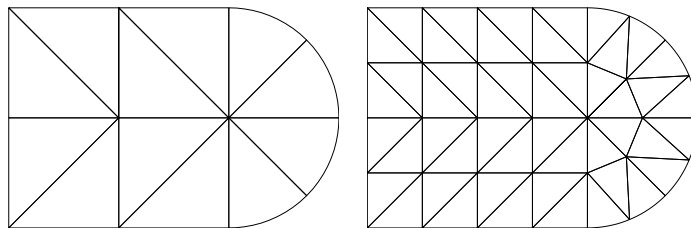
Figure 15. Coarse meshes for h-refinement test. Nested remeshing is used for refinement.

continuous formulation. If Dirichlet boundary conditions are imposed in strong form, an additional condition is required to keep optimal convergence rates: Fekette nodal distributions adapted to every curved element have to be considered, see right distribution in Figure 9. This is formally stated in the next result.

Theorem 2. *Under the assumptions of Theorem 1, the error bounds* (9) *and* (10) *hold for a NEFEM solution with a strong implementation of Dirichlet boundary conditions, if Fekette nodal distributions adapted for every curved element along the Dirichlet boundary are considered.*

The requirement of Fekete nodal distributions is necessary for an accurate interpolation of Dirichlet boundary conditions on curved boundaries. Due to the use of polynomial nodal basis in cartesian coordinates, the errors in the approximation of the prescribed value along the boundary may deteriorate the convergence of the solution. This is the case for NEFEM as well as for other approaches considering cartesian polynomial approximations. For instance, in [32] optimal convergence rates are proven when nodes on the boundary correspond to Lobatto points (i.e Fekette points in 1D).

4. NUMERICAL EXAMPLES

The application of the proposed methodology is illustrated using several numerical examples. The first example is an elliptic problem and it is solved using a continuous Galerkin formulation. More complex problems, concerning the numerical solution of transient Maxwell's equations, are also considered in order to illustrate the efficiency of NEFEM in a DG framework.

4.1. Poisson problem

The following model problem is solved in two dimensions

$$\begin{cases} -\Delta u & = & f & \text{in} & \Omega \\ u & = & u_d & \text{on} & \Gamma_d \\ \nabla u \cdot \boldsymbol{n} & = & g_n & \text{on} & \Gamma_n \end{cases} \qquad (11)$$

where Ω is the domain (see two NEFEM meshes in Figure 15), $\overline{\Gamma}_d \cup \overline{\Gamma}_n = \partial\Omega$ and $\boldsymbol{n}$ is the outward unit normal vector on $\partial\Omega$. The source is given by $f(x,y) = x\cos(y) + y\sin(x)$, such that the analytical solution of the problem is known and smooth,
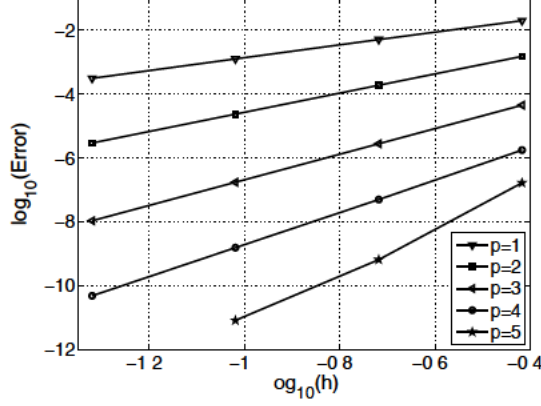
Figure 16. NEFEM h-convergence in the $\mathcal{L}^2(\Omega)$ norm for Poisson example

p	$\mathcal{L}^2$	$\mathcal{L}^\infty$	Energy
1	2.21	1.63	1.21
2	3.06	2.98	2.12
3	4.02	4.00	3.04
4	5.02	4.95	4.08
5	6.02	5.94	5.02

Table I. NEFEM h-refinement rates of convergence for Poisson example

$$u(x,y) = x\cos(y) + y\sin(x).$$

A Dirichlet boundary condition, corresponding to the analytical solution, is imposed in the polygonal part of the boundary Γ_d, and a Neumann boundary condition, also corresponding to the analytical normal flux, is imposed in the curved part of the boundary Γ_n. The curved part of the boundary, corresponding to half of a circle, is exactly described with NEFEM using one quadratic trimmed NURBS.

In order to check the theoretical convergence rates of Theorem 1, h-refinement is first explored. Figure 15 shows the first computational meshes, nested remeshing is used for refinement. The $\mathcal{L}^2(\Omega)$ error is plotted in Figure 16 for polynomials of degree up to $p = 5$. Table I also reports the rate of convergence in the $\mathcal{L}^2(\Omega)$ norm, the $\mathcal{L}^\infty(\Omega)$ norm and the energy norm. As stated in Theorem 1, NEFEM provides optimal convergence rates.

In this section, numerical integration is performed with $p + 1$ integration points for λ parameter, see Remarks 3 and 5. Thus, the number of integration points for the computation in a NEFEM element is the same as for a standard isoparametric FE.

Figure 17 shows a similar analysis but related to the Neumann boundary: h-convergence in the $\mathcal{L}^2(\Gamma_n)$ norm is compared for isoparametric FE and NEFEM with a polynomial interpolation up to degree $p = 3$. Optimal convergence rates, i.e $p + 1$, are obtained with isoparametric FE. The interior node for isoparametric curved FE with $p = 3$ is located following the algorithm in [28]. An algorithm to compute nodal coordinates for higher order isoparametric FE, not considered here, can be found in [29]. Further numerical experiments not
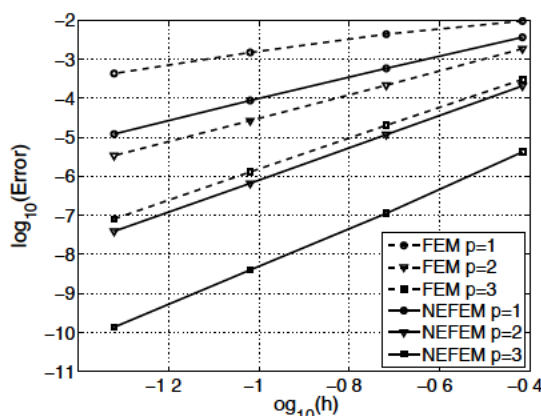
Figure 17. h-convergence in the $\mathcal{L}^2(\Gamma_n)$ norm for the Poisson example

reported here, confirm the importance of a proper location of interior nodes for isoparametric FE computations: clearly suboptimal rates of convergence are obtained for $p \geq 3$ if nodal coordinates are not located following [28, 29]. This is not the case for NEFEM, where optimal convergence rates are ensured for any interpolation degree and for any distribution of interior nodes in curved elements, see section 3.4.

Is it probably more important to note that this numerical experiment shows that NEFEM exhibits higher accuracy and rate of convergence for the $\mathcal{L}^2(\Gamma_n)$ norm. For instance, similar accuracy and convergence is obtained for quadratic isoparametric FE and for NEFEM with linear interpolation, with a saving in the number of nodes between 25% and 35%. Analogously, the error with cubic isoparametric FE is almost identical to the error with NEFEM using quadratic interpolation, with a saving in the number of nodes of about 50%. Moreover, for the same mesh and order of interpolation, NEFEM is between two and three orders of magnitude more precise than the corresponding isoparametric FE solution. Thus, this numerical example illustrates the efficiency of NEFEM, in front of isoparametric FE, for the computation of quantities of interest at (or near) curved boundaries. Similar conclusions are derived from the scattering simulations shown in section 4.2.

No significative differences between NEFEM and isoparametric FE accuracy are observed when the error is measured on the whole domain in $\mathcal{L}^2(\Omega)$ norm. As expected for an elliptic problem, the influence of the geometry of the boundary (or of boundary conditions) is inappreciable in the interior of the domain. This is not the case for instance for wave problems, where pollution errors may deteriorate the solution in the whole domain.

Next, a p-convergence study is performed using the computational meshes represented in Figure 15. As usual in the context of p and hp versions of the FEM, see [27, 33], the error in the energy norm is represented in Figure 18 as a function of the square root of the number of degrees of freedom. NEFEM, as expected from Theorem 1, presents exponential convergence.

It is important to remark that same conclusions are derived from all numerical tests in this section if Dirichlet boundary conditions are imposed along the curved boundary, with both a weak imposition, see Theorem 1, or with a strong imposition using Fekette points, see Theorem 2 and Figure 9.
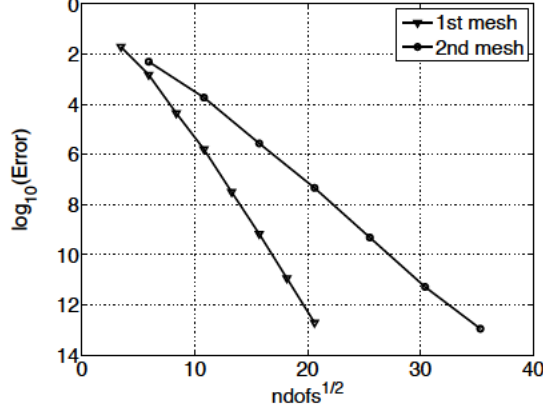
Figure 18. NEFEM p-convergence in the energy norm for Poisson example

Finally, it is worth noting that in a FE adaptive process, see [34], the computational mesh must be locally refined to properly account both for the solution and the geometry. Whereas in a NEFEM context the adaptive process is controlled only by the complexity of the solution, independently of the geometrical complexity of the domain, and therefore reducing the necessary number of degrees of freedom to achieve a desired accuracy.

4.2. Electromagnetic scattering simulations

In this section a DG formulation is considered for the simulation of 2D scattering of a single plane electromagnetic wave by a *Perfect Electric Conductor* (PEC) obstacle, assumed to be surrounded by free space. For a linear isotropic material of relative permittivity ε and relative permeability μ, 2D Maxwell's equations (which are decoupled in the *Transverse Electric*, TE, and *Transverse Magnetic*, TM, modes) can be written in dimensionless conservative form as

$$\frac{\partial U}{\partial t} + \frac{\partial F_k(U)}{\partial x_k} = 0 \qquad \text{in } \Omega, \tag{12}$$

where Einstein notation is assumed. The vector of conserved quantities U and the fluxes F_k are

$$U = \begin{pmatrix} \varepsilon E_1 \\ \varepsilon E_2 \\ \mu H_3 \end{pmatrix}, \quad F_1 = \begin{pmatrix} 0 \\ H_3 \\ E_2 \end{pmatrix}, \quad F_2 = \begin{pmatrix} -H_3 \\ 0 \\ -E_1 \end{pmatrix},$$

for TE mode, and

$$U = \begin{pmatrix} \varepsilon E_1 \\ \varepsilon E_2 \\ \mu H_3 \end{pmatrix}, \quad F_1 = \begin{pmatrix} 0 \\ H_3 \\ E_2 \end{pmatrix}, \quad F_2 = \begin{pmatrix} -H_3 \\ 0 \\ -E_1 \end{pmatrix},$$

for TM mode, where $E = (E_1, E_2, E_3)^T$ and $H = (H_1, H_2, H_3)^T$ are the *scattered* electric and magnetic field intensity vectors. It is assumed that there are no electric sources in the material.

In the DG implementation, numerical fluxes at the interior edges are defined from the Rankine-Hugoniot jump conditions [35], which can also be interpreted as a *flux splitting*
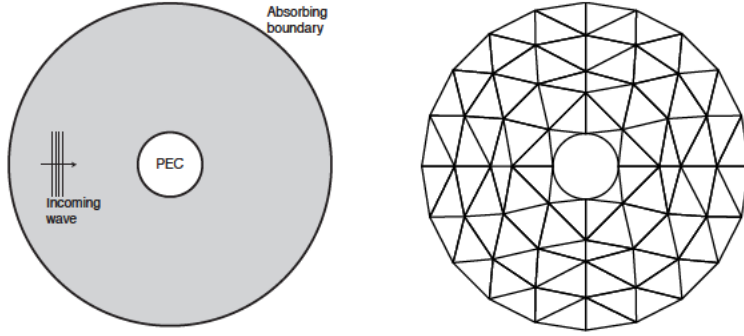
Figure 19. Scattering of a planar wave by a PEC cylinder: problem setup and computational mesh

technique, see [36]. Artificial absorbing boundaries are implemented with a first-order Silver-Müller condition, see for instance [37], and in all the examples computations are stopped before scattered waves reach the artificial boundary. Otherwise, more accurate artificial absorbing boundaries should be considered, see for instance [38]. At a PEC boundary, the tangential component of the total electric field (scattered plus incident) and the normal component of the total magnetic field vanish, that is

$$\boldsymbol{n} \times \boldsymbol{E} + \boldsymbol{n} \times \boldsymbol{E}^I = 0, \qquad \boldsymbol{n} \cdot \boldsymbol{H} + \boldsymbol{n} \cdot \boldsymbol{H}^I = 0,$$

where the superscript I refers to the incident wave. Using Rankine-Hugoniot jump conditions, PEC boundary conditions lead to the following numerical flux

$$\widehat{\boldsymbol{F}}_n^{\text{PEC}}(\boldsymbol{U}) = \begin{pmatrix} -n_2 H_3^{\text{PEC}} \\ n_1 H_3^{\text{PEC}} \\ -\alpha^I \end{pmatrix}, \qquad \text{where} \quad H_3^{\text{PEC}} = H_3 + \sqrt{\varepsilon/\mu} \left(\alpha + \alpha^I \right).$$

for TE mode, and

$$\widehat{\boldsymbol{F}}_n^{\text{PEC}}(\boldsymbol{U}) = \begin{pmatrix} n_2 E_3^{\text{PEC}} \\ -n_1 E_3^{\text{PEC}} \\ -\beta^I \end{pmatrix}, \qquad \text{where} \quad E_3^{\text{PEC}} = E_3 + \sqrt{\mu/\varepsilon} \left(\beta + \beta^I \right).$$

for TM mode, where $\alpha := n_1 E_2 - n_2 E_1 \equiv \boldsymbol{n} \times \boldsymbol{E}$ and $\beta := -n_1 H_2 + n_2 H_1 \equiv -\boldsymbol{n} \times \boldsymbol{H}$. All computations are performed using a fourth-order explicit Runge-Kutta time-marching scheme.

4.2.1. Circle: The first example considers an incident plane wave travelling in the x^+ direction and scattered by a circle, which is exactly described with a quadratic NURBS curve, see Figure 19. The diameter of the circle is two wave lengths. A coarse mesh with only four elements for the discretization of the NURBS boundary is considered and high-order approximations are used to properly capture the solution. To avoid ill-conditioning for high-order computations, all numerical solutions in this section are obtained with Fekette node distributions on both straight-sided and curved elements.

Figure 20 shows the transverse field H_3 and the *Radar Cross Section* (RCS) for TE mode, after four cycles, with a NEFEM approximation of degree 7. The NEFEM solution and the

(a) H_3 (b) RCS
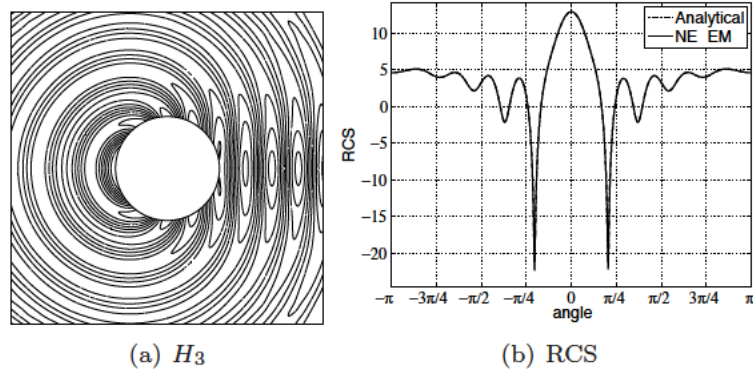
Figure 20. H_3 distribution and TE RCS after four cycles using NEFEM and $p = 7$

(a) 5th order   (b) 6th order
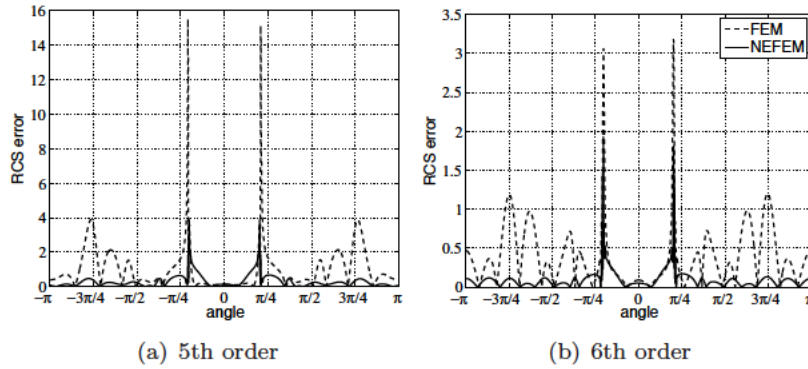
Figure 21. Comparison of TE RCS error distribution for FE and NEFEM with $p = 5, 6$

analytical solution [39] are overlapped; more precisely the $\mathcal{L}^2([-\pi, \pi])$ error in the RCS is $1.6\ 10^{-2}$, whereas the error for isoparametric FE is $6.1\ 10^{-2}$. Figure 21 shows a more detailed comparison: the RCS error distribution for isoparametric FE and for NEFEM using high-order approximation, namely $p = 5, 6$. In both cases, NEFEM clearly improves the solution. The same analysis is performed for TM mode. Figure 22 shows the E_3 distribution and the RCS for $p = 7$ on the coarse mesh depicted in Figure 19. Again, numerical and analytical solutions are overlapped. Moreover, the comparison with isoparametric FE in Figure 23 demonstrates, once more, the better performance of NEFEM.

To compare accuracy, the error evolution for increasing p is depicted in Figure 24. For the same discretization (i.e. same degree of interpolation) NEFEM results are more accurate than the isoparametric FE ones. For instance, NEFEM with degree $p = 5$, provides a RCS with an error of about 2%, whereas isoparametric FE require $p = 7$ to achieve a comparable accuracy (2.4 times more degrees of freedom than NEFEM).

As commented in section 3.4, the lower accuracy of isoparametric FE for high-order computations is due to two main facts: the piecewise polynomial approximation of the
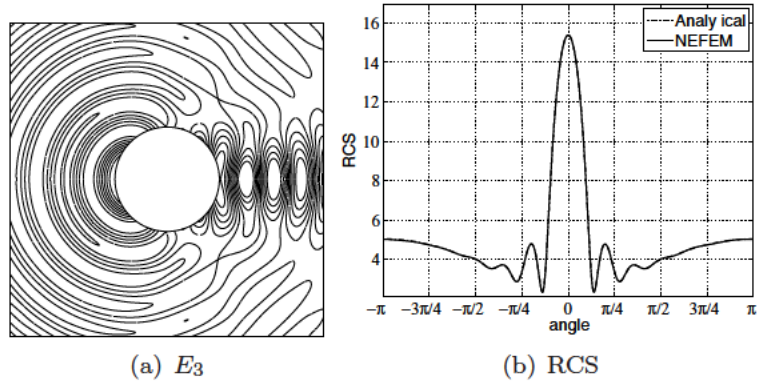
(a) E_3 (b) RCS

Figure 22. E_3 distribution and TM RCS after four cycles using NEFEM and $p = 7$

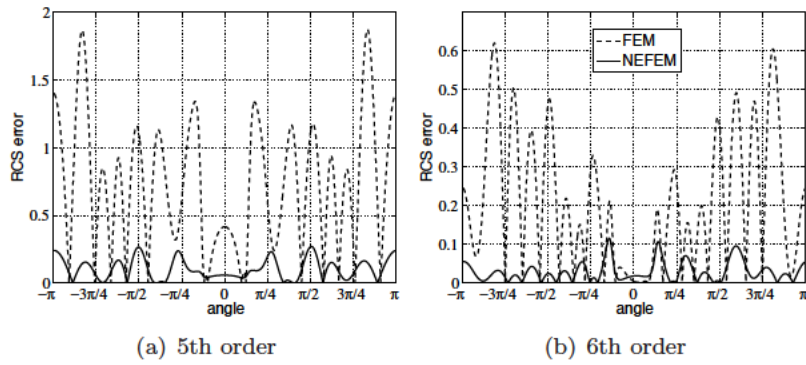(a) 5th order   (b) 6th order

Figure 23. Comparison of TM RCS error distribution for FE and NEFEM with $p = 5, 6$
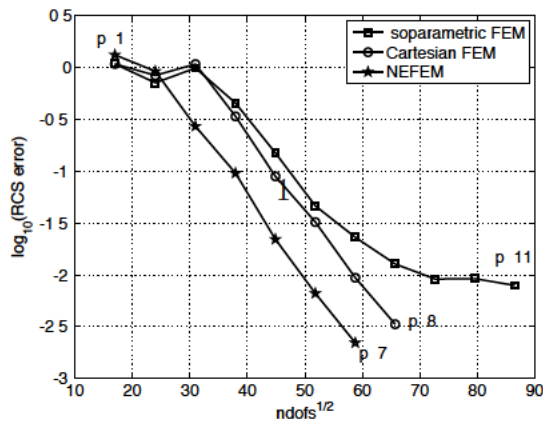

Figure 24. p-refinement convergence with the mesh in Figure 19. Markers are located for $p = 1, 2, 3, \ldots$

boundary, and the isoparametric transformation used to map the polynomial base in the reference element; which, for high-order approximation leads to a base in cartesian coordinates far from being polynomial. To quantify the effect of both sources of error, *cartesian FE* approximation is also considered and its accuracy depicted in Figure 24. That is, the usual reference element is used for integration purposes, but the polynomial base for the approximation of the solution is defined with cartesian coordinates directly in the physical domain. This means that an approximate (piecewise polynomial) description of the boundary is maintained, but the isoparametric transformation for the approximation is avoided. Thus, *cartesian FE* exactly reproduce polynomials in the physical domain. Similar results would be obtained using isoparametric FE with especially designed interior node coordinates instead of Fekette nodes, see [28, 29] and Sections 3.4 and 4.1.

Thus, the difference between the *cartesian FE* and NEFEM results in Figure 24 corresponds to the error due to the piecewise polynomial approximation of the boundary in a standard FE computation; which is completely eliminated in a NEFEM solution. More precisely, with NEFEM the outward normal vector is computed exactly in terms of the NURBS boundary parametrization, improving the flux computation at the PEC boundary.

Finally, it is important to note that NEFEM is a more efficient strategy than *cartesian FE*. The increase in the computational cost, due to the specific numerical treatment of curved elements along the boundary, is similar in NEFEM and *cartesian FE*, but from an accuracy point of view NEFEM provides much better results. For instance, the curves in Figure 24 show that to attain an accuracy comparable to a NEFEM computation with degree $p = 5$ (with an error of 2.2% in the RCS), *cartesian FE* require a discretization with degree $p = 6$ (with an error of 3.2%). That is, NEFEM provides similar accuracy to *cartesian FE* with a 63% reduction in the number of degrees of freedom.

4.2.2. NACA airfoil: The second example consists on the scattering of a planar wave by the NACA 0012 airfoil. The NACA 0012 is a symmetric airfoil with analytical expression [40], that can not be exactly described with a NURBS curve. As usual in the context of airfoil shape optimization, an approximation of the upper part of the airfoil using a B-Spline with eight control points is considered here, see for instance [22] for the B-spline data.

Figure 25 shows a detail of the computational mesh and the solution of TE mode with degree $p = 8$, for an airfoil with a chord length of 2 wave lengths. The angle of incidence is 0 rad. NEFEM E_3 distribution and the RCS are in good agreement with a reference numerical solution, see for instance [38], with an $\mathcal{L}^2([-\pi, \pi])$ error of 10^{-2} in the RCS. Figure 25 also shows the distribution of the error in the RCS for NEFEM and isoparametric FE, with Fekette nodal distributions. Again, NEFEM provides much more accurate results than isoparametric FE.

Next, NEFEM performance for a computation with higher frequency is tested: the NACA 0012 airfoil with a chord length of 10 wave lengths and angle of incidence of $\pi/2$ rad is considered, see for instance [41]. A detail of the computational mesh, and the NEFEM solution obtained with an approximation of degree $p = 13$ is shown in Figure 26. The E_3 field and the RCS are in good agreement with a reference solution, demonstrating the applicability of NEFEM methodology for the computation with high-degree approximation in coarse meshes (only 8 elements for the description of the airfoil boundary). The error distribution is also plotted in Figure 26. In this example the errors in the isoparametric FE solution are clearly unacceptable, whereas NEFEM demonstrates its good performance for
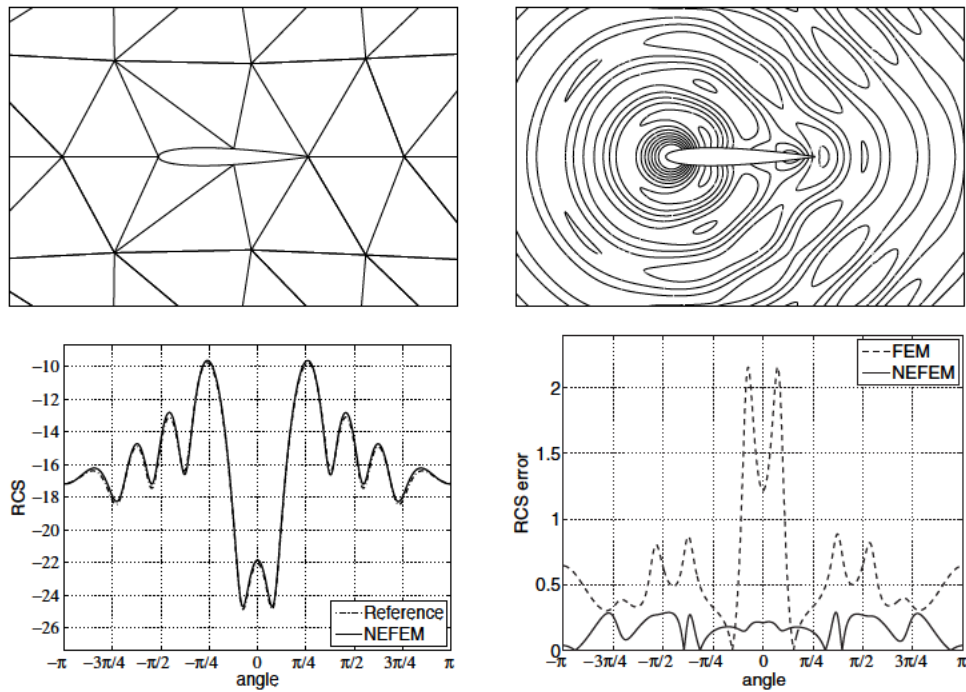
Figure 25. NACA 0012 airfoil with chord length of two wave lengths and angle of incidence of 0 rad ($p = 8$): detail of the computational mesh, H_3 distribution, RCS and error distribution.
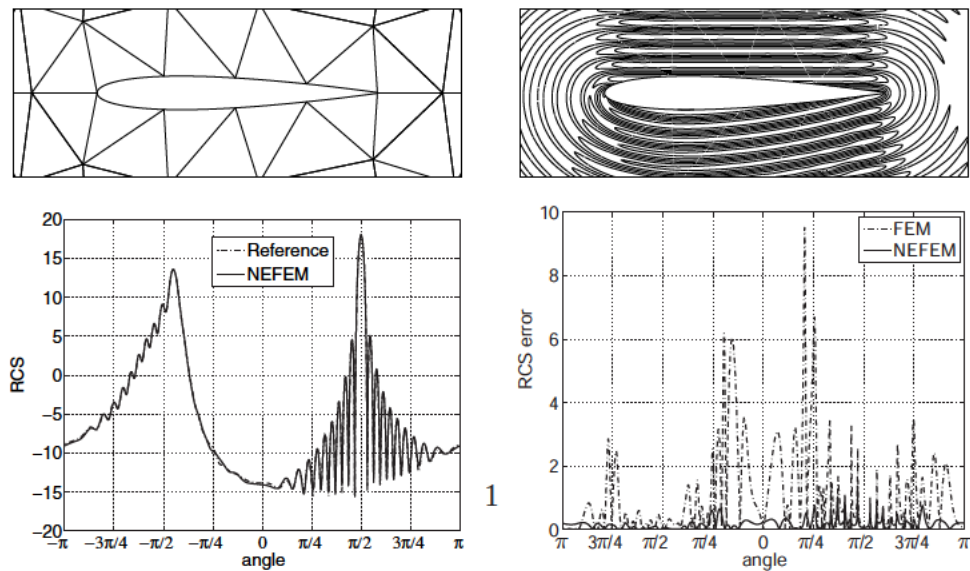

Figure 26. NACA 0012 airfoil with chord length of ten wave lengths angle of incidence of $\pi/2$ rad ($p = 13$): detail of the computational mesh, H_3 distribution, RCS and error distribution.
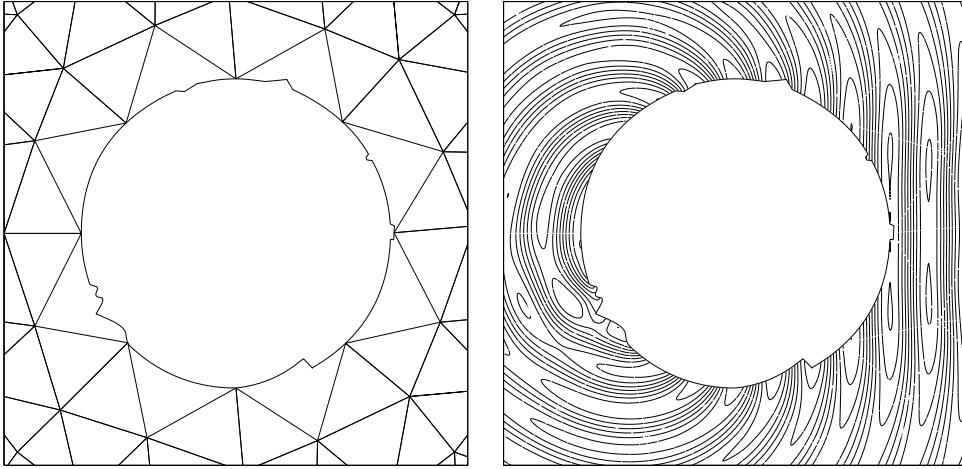
Figure 27. Irregular circle: detail of the computational mesh and NEFEM solution for $p = 9$.

high-order computations.

4.2.3. Complex scatterers: Previous examples show the advantages of the NEFEM formulation in front of classical FE for the numerical solution of some test cases. To illustrate all the capabilities of NEFEM, more complex scatterers are considered next. The first example is the scattering induced by an *irregular* circle with diameter of four wave lengths. The geometry of the obstacle is described *exactly* using one NURBS and a coarse mesh with only eight elements for the representation of the boundary is considered, see Figure 27.

As noted earlier, see section 3, it is important to remark that the only restriction for a NEFEM triangle is that the curved edge belongs to one NURBS. The computational mesh is chosen to emphasize the possibilities of NEFEM. It is not necessary to locate nodes at boundary corners (boundary points with $\mathcal{C}^0$ continuity), nor to refine the mesh near the boundary to capture the geometry (it is exactly represented in NEFEM independently of the spatial discretization!).

Figure 27 also shows the transverse field H_3 with $p = 9$ after four cycles. Even for elements with corners in its NURBS edge the quality of the solution is not deteriorated. Details showing the transverse field near the irregularities are represented in Figure 28.

The last example consists on the scattering of an electromagnetic wave by a real aircraft profile of ten wave lengths. The geometry of the 2D section of this aircraft has several critical zones, in particular, a small irregularity on the upper part and the rear part. Figure 29 shows the computational mesh used for NEFEM simulation, with only 44 elements on the curved boundary. Some details of the mesh are also represented, showing that it is not necessary to refine the mesh to capture exactly the geometry. Figure 30 shows the transverse field H_3 after ten cycles and some details near the most critical zones of the aircraft.

It is worth noting that using classical isoparametric FE it is not possible to compute accurate solutions for these problems with the computational meshes used by NEFEM, see Figures 27 and 29. To properly capture the geometry of the domain with isoparametric FE it is
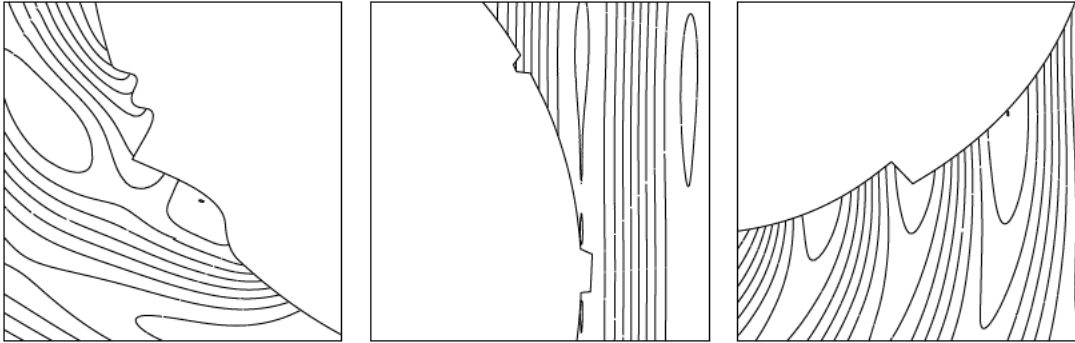
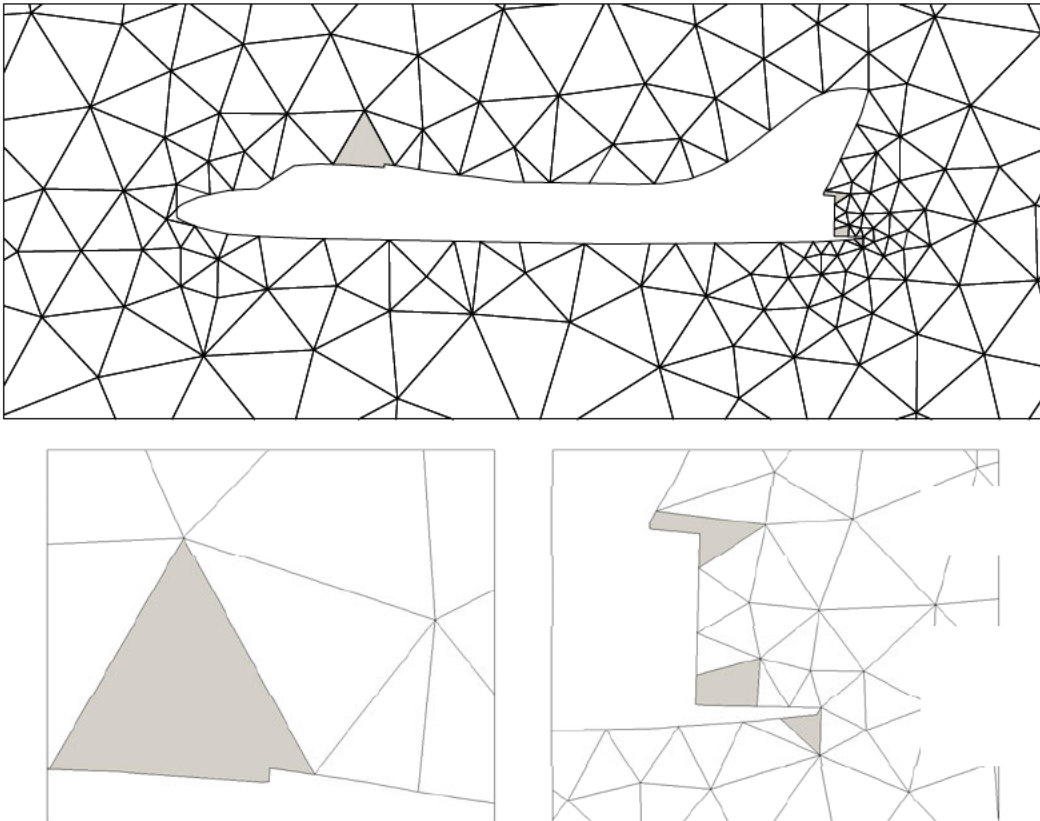Figure 28. Irregular circle: details of NEFEM solution near some irregularities.

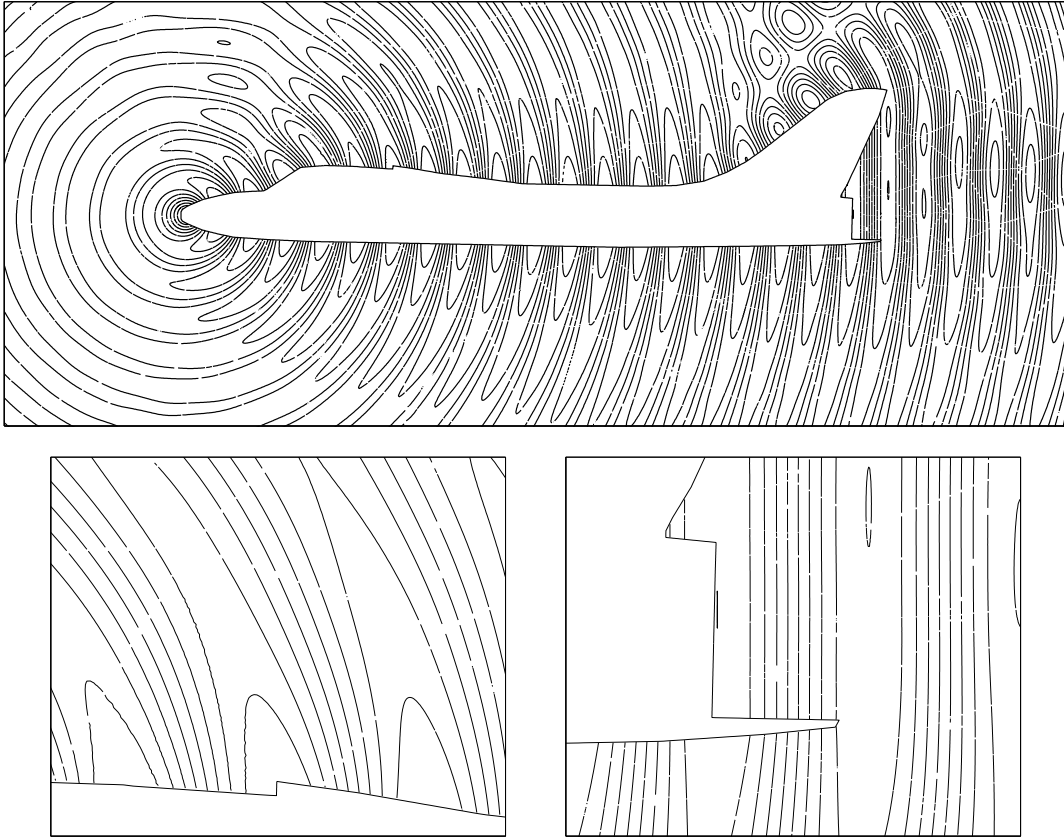Figure 29. Aircraft profile: details of NEFEM computational mesh.

Figure 30. Aircraft profile: details of NEFEM solution for $p = 8$ (H_3 distribution).

necessary to discretize accounting for corners nodes (boundary points with only $\mathcal{C}^0$ continuity). Thus, the minimum element size is controlled by the size of these irregularities, increasing the number of degrees of freedom in comparison with NEFEM. For instance, Figure 31 represents a computational mesh adapted to use isoparametric FE. Detailed views near critical zones of the aircraft show that h-refinement is mandatory to properly capture the slope discontinuities in the aircraft profile. The minimum mesh size for the FE mesh in Figure 31 is $3 \, 10^{-3}$ whereas the minimum mesh size for NEFEM mesh in Figure 29 is 0.2. Obviously, this drastic difference between minimum mesh sizes induces important differences in the time-step size when explicit time integrators are used and, therefore, shows another advantage of NEFEM.

5. Concluding remarks

An improvement of standard FE is proposed in this work. The exact CAD description of the geometrical model is considered, but only for the boundary of the computational domain. At
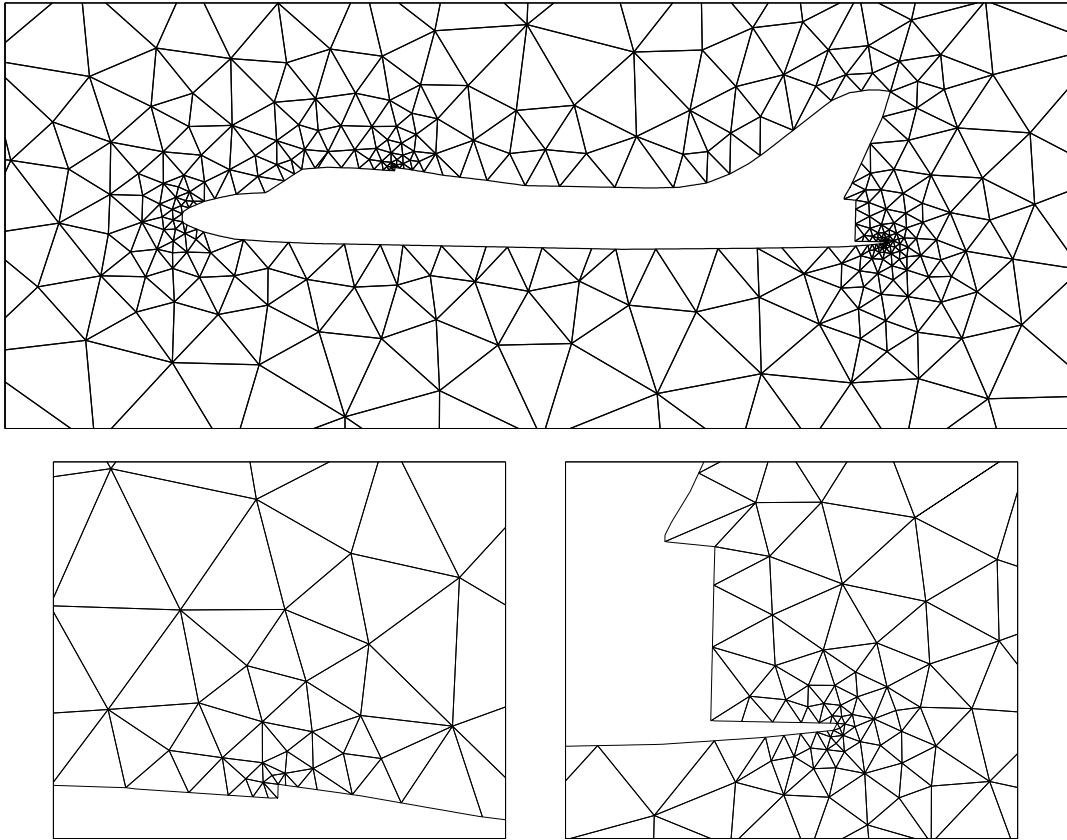
Figure 31. FE mesh around the aircraft profile and detailed view near critical zones

elements intersecting the NURBS boundary specific interpolation and numerical integration are proposed and, at elements not intersecting the boundary classical FE are used, preserving the efficiency of the finite element method. A priori error estimates are given and comments on the implementation of NEFEM are detailed. It is worth noting that a little effort is needed to enhance a usual FE code with the NEFEM concept.

Numerical examples demonstrate the advantages of NEFEM in front of classical isoparametric and cartesian FE. A Poisson example shows the applicability of the proposed method in a continuous Galerkin framework. Moreover, it allows to corroborate the a priori error estimates. Some electromagnetic scattering applications are used to show the benefits of the proposed method combined with a DG formulation. Even if the geometry of the boundary of the domain is simple, like a circle, NEFEM is, at least, one order of magnitude more precise than isoparametric FE. When the geometric model is complex, like and aircraft profile, NEFEM is able to compute accurate solutions using coarse meshes. The exact representation of the boundary allows to mesh the domain independently of the geometric complexity of the boundary whereas classical isoparametric FE need h-refinement to properly capture the

geometry.

REFERENCES

1. F. Bassi and S. Rebay, "High-order accurate discontinuous finite element solution of the 2D Euler equations," *J. Comput. Phys.*, vol. 138, no. 2, pp. 251–285, 1997.
2. T.J. Barth, *Simplified numerical methods for gas dynamics systems on triangulated domains.* PhD thesis, Department of Aeronautics and Astronautics, Stanford University, 1998.
3. X.J. Luo, M.S. Shephard, and J.F. Remacle, "Influence of geometric approximation on the accuracy of higher order methods," *SCOREC report*, vol. 1, 2001.
4. D. Xue and L. Demkowicz, "Control of geometry induced error in hp finite element (FE) simulations. I. Evaluation of FE error for curvilinear geometries," *Int. J. Numer. Anal. Model.*, vol. 2, no. 3, pp. 283–300, 2005.
5. H. van der Ven. and J.J.W. van der Vegt , "Space-time discontinuous Galerkin finite element method with dynamic grid motion for inviscid compressible flows: II. Efficient flux quadrature," *Comput. Methods Appl. Mech. Eng.*, vol. 191, no. 41–42, pp. 4747–4780, 2002.
6. L. Krivodonova and M. Berger, "High-order accurate implementation of solid wall boundary conditions in curved geometries," *J. Comput. Phys.*, vol. 211, no. 2, pp. 492–512, 2006.
7. B. Cockburn, *Discontinuous Galerkin methods for Computational Fluid Dynamics*, vol. 3 (Fluids) of *Encyclopedia of Computational Mechanics*, ch. 4. John Wiley & Sons, 2004.
8. A. Dadone and B. Grossman, "Surface boundary conditions for the numerical solution of the Euler equations," *AIAA Journal*, vol. 32, no. 2, pp. 285–293, 1994.
9. Z. J. Wang and Y. Sun, "A curvature-based wall boundary condition for the Euler equations on unstructured grids," in *Proceedings of the 40th AIAA Aerospace Sciences Meeting and Exhibit*, (Nevada), AIAA, 2002.
10. Z. J. Wang and Y. Liu, "Extension of the spectral volume method to high-order boundary representation," *J. Comput. Phys.*, vol. 211, pp. 154–178, 2006.
11. J.J. Muñoz, "Modelling unilateral frictionless contact using the null-space method and cubic B-Spline interpolation," *Comput. Methods Appl. Mech. Eng.*, 2007. In press.
12. T.J.R. Hughes, J.A. Cottrell, and Y. Bazilevs, "Isogeometric analysis: CAD, finite elements, NURBS, exact geometry and mesh refinement," *Comput. Methods Appl. Mech. Eng.*, vol. 194, no. 39–41, pp. 4135–4195, 2005.
13. L. Piegl and W. Tiller, *The NURBS Book*. London: Springer-Verlag, 1995.
14. F. Cirak, M. Ortiz, and P. Schröder, "Subdivision surfaces: A new paradigm for thin-shell finite-element analysis," *Int. J. Numer. Meth. Engrg.*, vol. 47, no. 12, pp. 2039–2072, 2000.
15. R. Sevilla, S. Fernández-Méndez, and A. Huerta, "NURBS-Enhanced Finite Element Method for Euler equations," *Int. J. Numer. Meth. Fluids*, 2007. Accepted.
16. J.S. Hesthaven and T. Warburton, "Nodal high-order methods on unstructured grids. I. Time-domain solution of Maxwell's equations," *J. Comput. Phys.*, vol. 181, no. 1, pp. 186–221, 2002.
17. G. Szegö, *Orthogonal Polynomials (fourth edition)*. Providence: Americam Mathematical Society, 1975.
18. Q. Chen and I. Babuška, "Approximate optimal points for polynomial interpolation of real functions in an interval and in a triangle," *Comput. Methods Appl. Mech. Eng.*, vol. 128, no. 3–4, pp. 405–417, 1995.
19. Q. Chen and I. Babuška, "The optimal symmetrical points for polynomial interpolation of real functions in the tetrahedron," *Comput. Methods Appl. Mech. Eng.*, vol. 137, no. 1, pp. 89–94, 1996.
20. M.A.Taylor, B.A. Wingate, and R.E. Vincent, "An algorithm for computing Fekete points in the triangle," *SIAM J. Numer. Anal.*, vol. 38, no. 5, pp. 1707–1720, 2000.
21. T. Belytschko, A. Huerta, S. Fernández-Méndez, and T. Rabczuk, *Meshfree methods*, vol. 1 (Fundamentals) of *Encyclopedia of Computational Mechanics*, ch. 10. John Wiley & Sons, 2004.
22. R. Sevilla and S. Fernández-Méndez, "Numerical integration for the 2D NURBS-Enhanced Finite Element Method," 2007. Submitted.
23. S. Wandzura and H. Xiao, "Symmetric quadrature rules on a triangle," *Comput. Math. Appl.*, vol. 45, no. 12, pp. 1829–1840, 2003.
24. S.C. Brenner and L.R. Scott, *The Mathematical Theory of Finite Element Methods*. New York: Springer, 1994.
25. P.A. Raviart and J.-M. Thomas, *Introduction à l'analyse numérique des équations aux dérivées partielles*. Paris: Dunod, 1998.
26. C. Johnson, *Numerical solution of partial differential equations by the finite element method*. Cambridge: Cambridge University Press, 1987.
27. B. Szabó and I. Babuška, *Finite Element Analysis*. New York: John Wiley & Sons, 1991.

28. P. G. Ciarlet and P. A. Raviart, "Interpolation theory over curved elements, with applications to finite element methods," *Comput. Methods Appl. Mech. Eng.*, vol. 1, no. 1, pp. 217–249, 1972.

29. M. Lenoir, "Optimal isoparametric finite elements and error estimates for domains involving curved boundaries," *SIAM J. Numer. Anal.*, vol. 23, no. 3, pp. 562–580, 1986.

30. J. Nitsche, "über ein variations zur lösung von dirichlet-problemen bei verwendung von teilräumen die keinen randbedingungen unterworfen sind," *Abh. Math. Se. Univ.*, vol. 36, pp. 9–15, 1970.

31. S. Fernández-Méndez and A. Huerta, "Imposing essential boundary conditions in mesh-free methods," *Comput. Methods Appl. Mech. Eng.*, vol. 193, 2004.

32. R. Scott, "Interpolated boundary conditions in the finite element method," *SIAM J. Numer. Anal.*, vol. 12, no. 3, pp. 404–427, 1975.

33. B. Szabó, A. Düster, and E. Rank, *The p-version of the Finite Element Method*, vol. 1 (Fundamentals) of *Encyclopedia of Computational Mechanics*, ch. 5. John Wiley & Sons, 2004.

34. A. Huerta, A. Rodríguez-Ferran, P. Díez, and J. Sarrate, "Adaptive finite element strategies based on error assessment," *Int. J. Numer. Meth. Engrg.*, vol. 46, no. 10, pp. 1803–1818, 1999.

35. R.J. LeVeque, *Numerical methods for conservation laws*. Lectures in Mathematics ETH Zürich, Basel: Birkhäuser Verlag, second ed., 1992.

36. J. Donea and A. Huerta, *Finite Element Methods for Flow Problems*. Chichester: John Wiley & Sons, 2002.

37. D. Givoli, *Numerical Methods for Problems in Infinite Domains*. Amsterdam: Elsevier, 1992.

38. P.D. Ledger, K. Morgan, O. Hassan, and N.P. Weatherill, "Arbitrary order edge elements for electromagnetic scattering simulations using hybrid meshes and a PML," *Int. J. Numer. Meth. Engrg.*, vol. 55, no. 3, pp. 339–358, 2002.

39. C.A. Balanis, *Advanced engineering electromagnetics*. New York: John Wiley & Sons, 1989.

40. C.L. Ladson, C.W. Brooks, A.S. Hill, and D.W. Sproles, "Computer program to obtain ordinates for naca airfoils," Tech. Rep. NASA TM-4741, NASA Langley Research Center, 1996.

41. J. Wu and B. Jiang, "A least-squares finite element mehod for electromagnetic scattering problems," Tech. Rep. ICOMP-96-12, NASA Lewis Research Center, 1996.